NOTICE

CERTAIN DATA CONTAINED IN THIS DOCUMENT MAY BE DIFFICULT TO READ IN MICROFICHE PRODUCTS.

2

CONF-9006153--4

UCRL-JC--103552

DE91 005423

An Optical Technique for the Direct Measurement of the 2-D Spectral Density of a Passive Scalar in a Turbulent Flow

H. F. Robey, G. F. Albrecht, and T. R. Moore

Prepared for presentation at the
AIAA 21st Fluid Dynamics, Plasma Dynamics, and Lasers Conference
Seattle, Washington
June 18-20, 1990

April 6, 1990

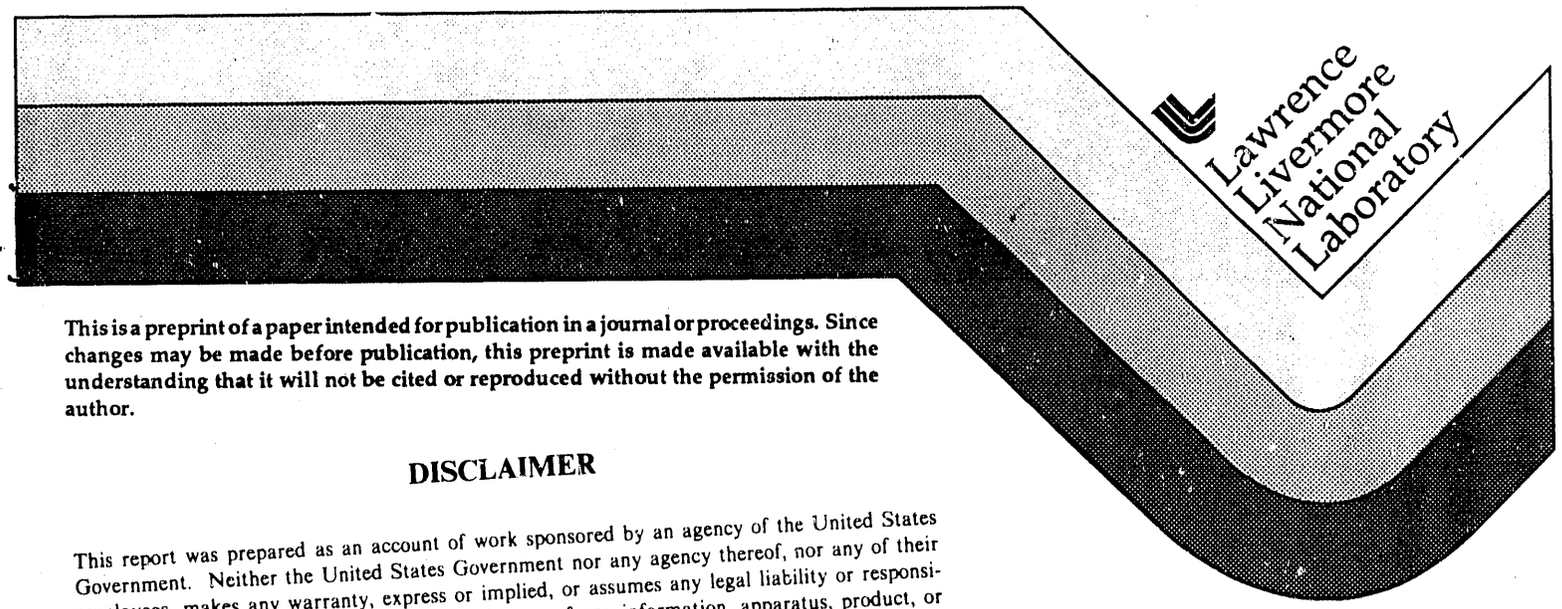

An Optical Technique for the Direct Measurement of the 2–D Spectral Density of a Passive Scalar in a Turbulent Flow

H. F. ROBEY, G. F. ALBRECHT, and T. R. MOORE

Lawrence Livermore National Laboratory, P. O. Box 808, Livermore, CA 94550

Abstract

A new optical technique for quantitatively measuring the spectral density of passive scalar fluctuations in a turbulent flow has been developed. The technique exploits the photorefractive properties of $BaTiO_3$ to separate the optical signal of the turbulent field from the coherent illumination background. It is a major improvement over existing techniques in that it is non–intrusive, has excellent frequency response and spatial resolution, and is capable of simultaneously measuring two components of the three–dimensional spectral density, $\Phi_\theta(\underset{\sim}{\kappa})$. The technique is thus especially well suited to the directly study of anisotropic flows. We have applied this technique to study the spectrum of temperature fluctuations in a fully developed turbulent channel flow with heat addition. The flow is highly anisotropic, yet the spectrum in directions transverse to the flow is seen to exhibit an inertial–convective subrange behavior which is characteristic of isotropic flows. The spectral behavior in the flow direction, due to the direct influence of the mean strain rate, is observed to be markedly different.

I. Introduction

A great deal of progress has been made over the years in understanding the mean properties of turbulent flows, but a detailed understanding of the statistical properties of the turbulent fluctuations still remains a great challenge. A recent review by Frisch and Orszag[1] points out the challenges to the theoretical, numerical, and experimental aspects of this problem. In that review, the authors called for "new turbulence experiments using state–of–the–art techniques borrowed from other branches of physics". The present paper presents such a technique.[2]

The new technique can instructively be viewed in relation to the well developed and widely used Schlieren technique. Though Schlieren has primarily been used for visualization of flow fields, its potential for directly obtaining turbulent spectra was recognized by Kopilevich[3,4], though his analysis required that the turbulence be isotropic. That restriction is not necessary in the present technique. The way in which a Schlieren setup can be used to study turbulent spectra is shown schematically in figure 1(a). The source of illumination is shown as a coherent beam for direct comparison with the present technique, but

for conventional Schlieren visualization it need not be coherent. The beam passes through a flow acquiring variations in the initially uniform phase. The phase variations are related to the integrated refractive index variations of the flow which may result from turbulent pressure fluctuations or, as in the present case, from isobaric temperature fluctuations.

The beam is brought to a focus with a positive lens forming an intensity distribution in the focal plane which, as is well known from Fourier optics, is the Fourier transform of the spatial intensity distribution in the aperture plane of the lens. For a limiting aperture at the lens which is rectangular, one obtains in the Fourier plane in the absence of flow and heat addition a background diffraction pattern such as that shown in figure 1(b).

The magnitude of the intensity which is scattered by the refractive index gradients in the flow is typically many orders of magnitude smaller than the background level. In order to visualize such gradients, some form of spatial filtering must be done to eliminate or reduce the background level. One of the simplest spatial filters, and indeed still one of the most commonly used, is a knife edge which is positioned either horizontally or vertically blocking out the primary arms of the diffraction pattern as shown in figure 1(c). In figure 1(c), well over 95% of the background intensity has been blocked by the knife edge, but the remaining portion is still much larger in magnitude than that scattered by the index field of the flow. Enough of the background has been removed, however, that index gradients can be visualized in the image plane as is done in a conventional Schlieren setup. The signal–to–background ratio is still too small to visualize the index field directly in the Fourier plane, though.

A partial view in the Fourier plane of the index field can be obtained by tailoring the spatial filter to the known form of the diffraction pattern as shown in figure 1(d). Here, enough of the background diffraction pattern has been spatially filtered out to allow the contribution from the perturbed index field to be visualized. It will be shown that this intensity distribution is directly proportional to the spectral density of the temperature fluctuations, $\Phi_\theta(\underset{\sim}{\kappa})$, of the flow. The obvious problem, however, is that the spatial filter mask physically blocks a significant portion of the Fourier plane intensity distribution and thus gives an incomplete picture of the spectrum.

Recent developments in the field of non–linear photorefractive optical materials allow us to overcome this problem. This is accomplished by replacing the spatial filter mask with a crystal of photorefractive $BaTiO_3$ located just before the beam focus. As will be shown, the $BaTiO_3$ acts as a temporal filter scattering out any portion of the beam which fluctuates on a time scale less than the crystal response time, τ_c. The background illumination which is ideally temporally invariant (this condition will be greatly relaxed later) sets up a volume diffraction grating in the crystal which effectively scatters this portion of the beam from the propagation path resulting in a reduction in focal plane background intensity of order 10^3. This allows the light scattered by the index gradients of the flow, which pass through the $BaTiO_3$ unattenuated, to be visualized directly in the Fourier plane with no spatial obstruction.

II. The Experimental Aparatus

The experimental aparatus is shown in figure 2. The beam from a Quantronix model 114 frequency doubled Nd:YAG laser operating at $\lambda = 532nm$ with very nearly diffraction limited beam quality is expanded with a 30 cm negative lens and propagated through a section of heated turbulent channel flow confined by optical quality windows which are oriented at the Brewster angle with respect to the incident beam. The Q-switched pulse length of ≤ 100 ns was short enough to effectively freeze the motion of the flow which was typically at a mean velocity of 35 m/s. The repetition rate of the laser was 1 kHz which allowed for the ensemble averaging of a large number of essentially instantaneous recordings of the spectral density, $\Phi_\theta(\underset{\sim}{\kappa})$. As will be shown, by varying this ensemble averaging time, one can controllably emphasize different wavenumber portions of the spectrum.

The transmitted beam is focussed by a 15 cm focal length lens through a $BaTiO_3$ crystal located approximately 2 mm in front of the focal plane. The focal spot is then magnified and re-imaged onto a diffuse screen from which it is photographed on Kodak p3200 film. The focal plane intensity distribution was recorded with different exposure times and with the insertion of various neutral density filters to enhance or supress various wavenumber portions of the spectrum. A calibration wedge of linearly increasing optical density was also photographed on the film and was used to convert the film density to intensity. The film was then digitized with a microdensitometer and processed as digital images.

Two $BaTiO_3$ crystals were used in the present experiments, both obtained from Sanders Associates. The first crystal, measuring $(5mm)^3$ was cut with its faces oriented at 45° to the $\hat{c}$–axis, while the second one measuring 7 x 7 x 6 mm^3 had faces cut parallel to the $\hat{c}$–axis. For the present experiments, the two crystals were used in series. The novel optical properties of $BaTiO_3$ rely on its ability to provide photorefractive amplification to light initially scattered from the random inhomogeneities or imperfections in the crystal lattice. This process is called stimulated photorefractive scattering (SPS), and its properties have been extensively investigated in recent years. It has been used in numerous applications such as phase conjugation[5], single beam interferometry[6], and optical time differentiation[7]. The photorefractive effect originates from the migration of movable charges (either electrons or holes or both) due to the presence of a non–uniform intensity field. The space charge field thus created then modulates the refractive index field of the crystal through the electro–optic effect. The microscopic details of this process are not entirely understood, however, and can vary widely from sample to sample. The value of the photorefractive gain coefficient, Γ_0, has been observed to depend strongly on impurity levels[8] and can be altered by reduction and oxidation at elevated temperatures[9]. For the present applications, however, only the macroscopic properties of the material will be important.

The use of $BaTiO_3$ as a high–pass temporal filter can be understood by considering the interaction of an incident beam, which will be taken as temporally invariant (cw) for the present and a single scattered component. (In practice, the process of SPS simultaneously occurs with many beams of scattered light and gives the appearance of "fanning" of the beam as it traverses the crystal[10].) The incident beam has intensity I_i and wave number vector $\underset{\sim}{\kappa}_i$, and the scattered beam has a time dependent intensity $I_s(t)$ and wave number $\underset{\sim}{\kappa}_s$. The difference in intensity of these two beams is the intensity transmitted through

the crystal, $I_T(t)$, which is also time dependent. The interference pattern generated by the spatial overlap of these two beams within the crystal produces a diffraction grating or volume hologram of wave number $\underset{\sim}{\kappa}_g$ as shown in figure 3. For an incident beam which is stationary in both space and time, this grating will grow exponentially, scattering a very large fraction of the incident beam into the scattered wave and thereby strongly depleting the transmitted intensity, I_T.

The exchange of energy between the two beams is described by a set of coupled wave equations, and the solution can be expressed in terms of the transmitted intensity as[6,11]

$$\frac{I_T(t)}{I_i} = \frac{(1+m_0)}{[1+m_0 e^{\Gamma(t)\cdot L}]} \tag{1}$$

where $m_0 = I_s(0)/I_i$ is the initially scattered fraction of the incident beam. L is the interaction length of the two beams within the crystal, and $\Gamma(t)$ is the effective photorefractive gain coefficient and is given by

$$\Gamma(t) = \Gamma_0(1 - e^{-t/\tau_c}) \tag{2}$$

The photorefractive response time of the crystal, τ_c, depends on the properties of the crystal such as impurity levels and method of preparation and also on the intensity of the laser. It can in principal be varied from milliseconds to hours.

For a cw beam whose intensity varies on a time scale which is long compared with τ_c, equation (1) for the transmitted intensity becomes

$$I_T(t >> \tau_c) \approx \frac{I_i}{[1+m_0 e^{\Gamma_0 \cdot L}]} \tag{3}$$

Typical values of Γ_0 for properly prepared crystals are on the order of 2 - 4 mm^{-1} resulting in very large amplification of the scattered beam and correspondingly large depletion of the transmitted beam. In the present experiments, the depletion of the transmitted beam was measured in the absence of flow and heat addition and was found to be approximately 10^{-3} when one crystal was used and 10^{-5} when two crystals were used in series.

In the present setup, a pulsed laser is used to freeze the motion of the flow. The analysis for a cw beam applies equally well in this case since the grating decay rate in the absence of any applied optical field (the dark space–charge recombination rate) is slow, varying from seconds to hours. The exact value of the dark decay rate again depends very strongly on material properties, method of preparation of the sample, and the value of the grating wavenumber, $\underset{\sim}{\kappa}_g$, as discussed in detail in [9]. In the present experiments, the repetition rate of the laser was 1 kHz, so the grating written by one pulse experiences negligible decay in the 1 ms dark interval before the next pulse. The depletion of the transmitted beam in this case approximately follows equation (1) with the appropriate time being the integrated "on" time of the beam, $t_{on} = ft$, where f is the duty cycle of the laser. The duty cycle can be absorbed into τ_c in equation (2) giving an effective crystal response time of τ_c/f. In the present experiments, this effective response time was approximately 1 second.

In contrast to the unperturbed beam, the spatially and temporally incoherent phase and amplitude fluctuations generated from the turbulent index field of the flow evolve on a time scale which is much shorter than τ_c. The largest eddys in the flow, for example, are on the order of 4 mm and are moving at a mean velocity of 35 m/s. They generate temporal variations on the beam which have a time scale on the order of $100\mu s$. Smaller flow structures have correspondingly smaller time scales. The scattering that these components generate within the crystal experiences very little amplification since (1) the grating written with each pulse is not reinforced by subsequent pulses due to the spatial and temporal incoherence, and (2) the incident intensity of these fluctuating components is many orders of magnitude smaller than that of the unperturbed beam. For these components, $t << \tau_c$, and equation (1) reduces to

$$I_T(t << \tau_c) \approx I_i \tag{4}$$

That is, for times short compared to the photorefractive response time, the beam traverses the crystal essentially unchanged.

III. Channel Flow Facility and Flow Documentation

The particular flow under study is shown schematically in figure 4. It consists of two 4 mm wide channels on either side of a center divider plate. The center divider was an optical quality ($\lambda/10$) quartz window which was heated on each side by an indium–tin–oxide (ITO) thin film resistive coating which could produce a surface heat flux of up to $5W/cm^2$. The outer walls also had optical quality windows allowing for the use of a number of optical diagnostics. The flow in each channel was a fully developed turbulent channel flow of N_2 at room temperature and 2 atm absolute pressure. The mean velocity was typically on the order of 35 m/s giving a Reynolds number based on the channel width D of 16,300.

The flow was extensively documented both experimentally and numerically. Figure 5(a) shows a typical velocity profile measured with a TSI model 1260A hot–wire and IFA–100 anemometer bridge circuit. Also shown is the velocity profile which was calculated numerically using the computer code TEXSTAN.[12] TEXSTAN numerically integrates the boundary layer form of the Navier–Stokes equations employing a two equation ($K - \epsilon$) closure model for the turbulence. Further details of the use of TEXSTAN for numerically calculating the flow in the present experimental configuration is given in [13]. The agreement between calculation and experimental measurements in Figure 5(a) is seen to be quite good.

The thermal properties of the flow were studied as well. Figure 5(b) shows the downstream development of the thermal boundary layer. The ITO heater on one side of the center divider was painted black to maximize its emissivity, and its temperature was measured with a Hughes "Probeye" infrared camera. The flow in this case was viewed through an IR–transparent saphire window. The rapid development of the thermal boundary layer is seen to occur within the first few cm, and after that the flow is thermally fully developed with the temperature increasing linearly due to the caloric heat addition. Again the

agreement between the experimental measurements and numerical calculations is good.

The region of the flow which was studied in the present experiments was located approximately 20 cm or 50 channel widths from the channel entrance nozzle as shown in Figure 4. The mean flow properties are slowly varying at this point and can be considered to be locally homogeneous in the two directions parallel to the walls. In the direction normal to the channel walls, of course, the flow is not homogeneous due to the boundary layers. The diameter of the diagnostic beam at this point is approximately 4 mm. The volume of the flow which is measured is therefore a cylinder 4 mm in diameter by 4 mm in length. It is important to recognize that there is no spatial resolution in the direction of beam propagation. The index field in this direction is integrated along the beam path. In the two transverse directions, however, the resolution is limited only by the F–number of the lens which forms the spectrum in the focal plane.

IV. Propagation and Scaling Considerations

The refractive index field of the flow is directly related to the density fluctuations through the Gladstone–Dale constant β_s (defined at standard conditions $P_s = 1atm, T_s = 20°C$) as

$$\Delta n(\underline{x},t) = \beta_s \frac{\Delta\rho(\underline{x},t)}{\rho_s} \tag{5}$$

The source of the density fluctuations can be either from isentropic turbulent pressure fluctuations or from temperature variations in the flow. Turbulent pressure fluctuations scale with the square of the fluctuating turbulent velocity field as

$$\Delta p \sim \rho_0 (u')^2 = \gamma P_0 \frac{(u')^2}{U_0^2} M^2 \tag{6}$$

The velocity fluctuation level is typically of order 10%, and the Mach number of the present flow is 0.1 giving a $\Delta\rho/\rho_0 = \gamma\Delta P/P_0$ of order 10^{-4}.

By contrast, the isobaric temperature fluctuations are much larger. From Figure 5, for example, the wall temperature rise is approximately $30°C$. This produces an isobaric density variation of $\Delta\rho/\rho_0 = -\Delta T/T_0 \approx 10^{-1}$, which is much greater than that resulting from pressure fluctuations. The refractive index field is then given by

$$\Delta n(\underline{x},t) = -\beta_s \left(\frac{\rho_0}{\rho_s}\right) \frac{\Delta T(\underline{x},t)}{T_0} = \text{const} \cdot \Delta T(\underline{x},t) \tag{7}$$

The fluctuating refractive index field is thus linearly proportional to the fluctuating temperature field. The magnitude of $\Delta n(\underline{x},t)$ is very small. For the present conditions, $\rho_0/\rho_s = 2$, $|\Delta T/T_0|_{\max} = 0.1$, and $\beta_s = 2.97\text{x}10^{-4}$ giving $|\Delta n|_{\max} \approx 5.9\text{x}10^{-5}$.

As the diagnostic beam traverses this perturbed refractive index field, it acquires transverse variations in its initially uniform phase. Amplitude variations also arise as the

beam propagates due to focussing and defocussing of this perturbed wave. The electric field of the beam can be written as a perturbation series of the form:

$$E = E_0 + E_1 + ... \tag{8}$$

where E_m is of order of smallness, $n_1^m = (\Delta n)^m$. It is easily shown[14] that the first order term, E_1, can be written as

$$\frac{E_1}{E_0} \approx \frac{A_1}{A_0} + i(s - s_0) \tag{9}$$

The observed amplitude and phase are, therefore, simply the real and imaginary parts of the perturbed electric field.

At this point, we must recognize that $A_1(\underset{\sim}{x})$, $s_1(\underset{\sim}{x})$, and $n_1(\underset{\sim}{x})$ are all spatially random functions and we must therefore deal with averaged properties. Following the standard notation, we define the following spatial autocorrelation functions :

$$B_A(\underset{\sim}{x}) = < A_1(\underset{\sim}{x}_1 + \underset{\sim}{x}) A_1(\underset{\sim}{x}_1) > \quad , \quad \underset{\sim}{x} = (x, y) \tag{10a}$$

$$B_s(\underset{\sim}{x}) = < s_1(\underset{\sim}{x}_1 + \underset{\sim}{x}) s_1(\underset{\sim}{x}_1) > \quad , \quad \underset{\sim}{x} = (x, y) \tag{10b}$$

$$B_n(\underset{\sim}{x}) = < n_1(\underset{\sim}{x}_1 + \underset{\sim}{x}) n_1(\underset{\sim}{x}_1) > \quad , \quad \underset{\sim}{x} = (x, y, z) \tag{10c}$$

and their respective Fourier transforms :

$$F_A(\underset{\sim}{\kappa}) = \frac{1}{(2\pi)^2} \int_{-\infty}^{\infty} \int_{-\infty}^{\infty} B_A(\underset{\sim}{x}) e^{-i\underset{\sim}{\kappa} \cdot \underset{\sim}{x}} d^2\underset{\sim}{x} \tag{11a}$$

$$F_s(\underset{\sim}{\kappa}) = \frac{1}{(2\pi)^2} \int_{-\infty}^{\infty} \int_{-\infty}^{\infty} B_s(\underset{\sim}{x}) e^{-i\underset{\sim}{\kappa} \cdot \underset{\sim}{x}} d^2\underset{\sim}{x} \tag{11b}$$

$$\Phi_n(\underset{\sim}{\kappa}) = \frac{1}{(2\pi)^2} \int_{-\infty}^{\infty} \int_{-\infty}^{\infty} \int_{-\infty}^{\infty} B_n(\underset{\sim}{x}) e^{-i\underset{\sim}{\kappa} \cdot \underset{\sim}{x}} d^3\underset{\sim}{x} \tag{11c}$$

$F_A(\underset{\sim}{\kappa})$ and $F_s(\underset{\sim}{\kappa})$ are the 2–D power spectral densities of the amplitude and phase of the perturbed electric field and their sum is the 2-D power spectral density of the intensity field. This is exactly the quantity that is measured in the focal plane behind the $BaTiO_3$ crystal.

Following the analysis in [14], it can be shown that $F_A(\underset{\sim}{\kappa})$ and $F_s(\underset{\sim}{\kappa})$ are related to $\Phi_n(\underset{\sim}{\kappa})$ by :

$$\begin{bmatrix} F_A(\underset{\sim}{\kappa}) \\ F_s(\underset{\sim}{\kappa}) \end{bmatrix} = \pi k^2 z \left(1 \mp \frac{k}{\kappa^2 z} sin \frac{\kappa^2 z}{k} \right) \Phi_n(\underset{\sim}{\kappa}, 0) \quad , \quad \underset{\sim}{\kappa} = (\kappa_x, \kappa_y) \tag{12}$$

where k is the wave number of the optical beam, and z is the length of the propagation path through the turbulent medium. The spectral density of the perturbed intensity field for $z = L$ is given by

$$F_I(\underset{\sim}{\kappa}) = F_A(\underset{\sim}{\kappa}) + F_s(\underset{\sim}{\kappa}) = \pi k^2 L \Phi_n(\kappa_x, \kappa_y, 0) = \text{const} \cdot \Phi_n(\kappa_x, \kappa_y, 0) \tag{13}$$

The important result is that the 2-D power spectral density of the measured intensity field is directly proportional to the two transverse components of the spectral density of the refractive index field which in turn is proportional to the spectral density of the fluctuating temperature field.

V. Discussion of the Data

Figure 6 shows several photographs of the focal plane intensity distribution which will henceforth be referred to as the 2-D spectral density or simply the spectrum of the temperature fluctuations. The photographs were taken with different exposure times to bring out different wave number portions of the spectrum. Figures 6(a,b) were taken with exposure times of 1/8 second and 4 seconds, respectively. Neutral density filters with an attenuation of 10^{-2} were used in these photographs as well to limit the transmitted intensity to the low wave number portion of the spectrum. In Figure 6(c), the exposure time was 16 seconds and the neutral density filters were removed in order to bring out the higher wave number part of the spectrum. In all cases, the surface heat flux was $4W/cm^2$. Note the change in scale from 6(a,b) to 6(c). Also note the appearance in 6(c) of the irregular asymmetric scattering on the right side of the photograph. This is a portion of the photorefractive fanout of the coherent beam scattered by SPS.

In each case, the photographs were digitized with a physical resolution on the film of $13\mu m$. The magnification of the focal plane onto film was 12.5 x, so the spatial resolution in the focal plane was approximately $1\mu m$. The axes in Figure 6 are shown in terms of the actual spatial dimensions in the focal plane as well as the normalized transverse wave numbers of the thermal structures in the flow, $\kappa_x D$ and $\kappa_y D$. The flow is in the x-direction.

The short exposure times such as Figures 6(a,b) enhance the visualization of the lowest wavenumber part of the spectrum, since that part of the spectrum contains the bulk of the turbulent energy and therefore generates the largest contribution to the scattered spectrum. The two well defined peaks at $\kappa_y D \approx \pm 2\pi$ correspond to flow structures with a dominant transverse wavelength equal to the channel width, i.e. the largest possible scale of motion. Note that the scattered intensity decreases for wave numbers smaller than this. It is important to note that the peak in the energy spectrum is not observed using conventional one-point measurement techniques such as a hot-wire, since such measurements suffer from aliasing at low wave numbers. In the present technique aliasing is not a problem. This enables us for the first time to study the low wave number behavior directly.

The flow structures corresponding to this part of the spectrum are clearly anisotropic with the scattered spectrum being at least 3 times wider in the transverse direction than in the flow direction. This corresponds to turbulent thermal eddies which are alligned with the flow and are 3 times longer in the flow direction than in the transverse direction. This anisotropy is due to the straining of the mean flow on the turbulent structures.

The higher wave number portion of the spectrum is obtained by taking a longer time exposure as shown in Figure 6(c). Due to the finite dynamic range of the film, the lower wave number region is saturated, but the behavior in the higher wave number regime can

now be seen. Note that the degree of anisotropy is seen to be reduced for the smaller, higher wave number, structures (approximately 1.4:1), but full isotropy has still not been reached. A fully isotropic spectrum would have contours which are circular, and it is seen in Figure 6(c) that the spectrum is tending toward this asymptotic form as $|\underset{\sim}{\kappa}| \rightarrow \infty$. The smallest structures shown in the spectrum of Figure 6(c) with $\kappa_y D = 124$ correspond to thermal eddys which are approximately 20 times smaller than the channel width or $200\mu m$. Such spatial resolution is well beyond the limits of a hot–wire but could be obtained by an LDV measurement. This points out an important distinction. A hot–wire or an LDV measurement is a point measurement, and has a spatial resolution limit which depends on the size of the hot–wire or LDV measurement volume. The present technique, on the other hand, is a measurement over a volume. Within that volume, however, very small scales can be resolved with the resolution being limitted only by the ability of the focussing lens to capture the wider angle scattering caused by the smaller structures.

One of the unique features of this technique is that one can now look at the behavior of turbulent spectra as a function of direction. Figure 7, for example, shows the directional spectra in the transverse (y) and longitudinal (x) directions as obtained from the data of Figure 6(c). The two spectra are plotted on a log–log scale, and it is seen that there is a difference in the slope of the two curves indicating a different power law dependence. In the transverse direction, the slope is –11/3. This can be compared with the more commonly plotted spectra of the isotropic scalar function, $\Gamma(\kappa)$, which is the energy of the scalar fluctuations as a function of wave number magnitude. Since it is a scalar function, $\Gamma(\kappa)$ is only applicable to purely isotropic flows such as grid turbulence or to limited regions of anisotropic spectra where the flow can be considered to be locally isotropic. Obukhov[15] and Corrsin[16] showed that for a locally isotropic flow, $\Gamma(\kappa)$ exhibited an inertial–convective subrange behavior in which $\Gamma(\kappa) \sim \kappa^{-5/3}$.

For an isotropic flow, $\Gamma(\kappa)$ and $\Phi_\theta(\underset{\sim}{\kappa})$ can be directly related by integrating $\Phi_\theta(\underset{\sim}{\kappa})$ over a spherical shell of radius κ to remove the directional dependence:

$$\Gamma(\kappa) = \int\int \Phi_\theta(\underset{\sim}{\kappa}) d\sigma \tag{14}$$

where $d\sigma$ is the elemental area of the surface. From (14) the corresponding form of the spectral density in the inertial–convective subrange is $\Phi_\theta(\kappa) \sim \kappa^{-11/3}$. This is exactly the slope that is observed for the transverse spectrum in Figure 7, though the present flow is far from being isotropic. The reason for this similarity is believed to be a consequence of the fact that the wave number dependence of the spectrum is a function of the strain rate field of the flow (see extensive discussion in reference [17]). In the transverse direction, there is no mean strain rate component. The eddys therefore evolve essentially as though they were in an isotropic flow.

In the flow direction, however, the mean strain rate dominates the fluctuating strain rate at low wave numbers, and it can be shown by dimensional analysis[17] that $\Phi_\theta(\kappa_x) \sim \kappa_x^{-9/3}$ as is observed in figure 7. This slope will be observed only in the flow direction, x, as that is the only direction in which a mean strain rate component exists. This anisotropy in the two spectra of Figure 7 is able to persist because in the time that it takes to rotate a longitudinal eddy into the transverse direction, it will have equilibrated with the fluctuating strain rate and will have transferred its energy to smaller scales.

Figure 7 therefore identifies a new region of the inertial–convective subrange, the anisotropic equilibrium range, in which the longitudinal eddys receive energy directly from the mean flow and are in equilibrium with the mean strain rate rather than the turbulent strain rate field. The spectral dependence for the longitudinal and transverse directions is therefore different. Note that this observation relies on the ability to measure the spectral density directly and could not have been made with conventional one point measurements techniques. This observation enables us to generalize the notion of an energy cascade to include the low wave number, anisotropic part of the spectrum, and allows us for the first time to directly and simply obtain the spectrum of anisotropic turbulent flows of practical engineering significance.

VI. Conclusions

A new optical technique has been presented for quantitatively measuring the spectral density of scalar fluctuations in a turbulent flow. Initial experiments on a heated turbulent channel flow have demonstrated several of the unique capabilities of this technique including (1) the resolution, free of aliasing, of the low wave number part of the spectrum, (2) the observation of an "isotropic" inertial–convective subrange behavior in the transverse direction, and (3) the observation of the mean strain dominated, anisotropic equilibrium range in the longitudinal spectrum. All of these observations are made possible by the ability to obtain the 2–D spectral density directly rather than just the 1–D isotropic spectral function. This technique now makes possible the study of a very wide class of anisotropic flows of considerable practical interest.

Future experiments are currently being planned to exploit the high spatial resolution to directly study the dissipation region of the spectrum. Further experiments also include the study of the effects of strain rate, rotation rate, and shear on the development of an anisotropic spectrum. The technique is also easily extended to obtain all three components of the spectral density by employing two mutually perpendicular beams. In conclusion, we expect this technique to provide a wealth of new insights into the structure of turbulent flows and to greatly contribute to our knowledge of this important subject.

Acknowledgements

This work was performed under the auspices of the U.S. Department of Energy by Lawrence Livermore National Laboratory under Contract No. W–7405–Eng–48.

References

1. U. Frisch and S. A. Orszag, Physics Today **43** (1) (1990).

2. G. F. Albrecht, H. F. Robey, and T. R. Moore, submitted to Applied Physics Letters, January (1990).

3. Y. I. Kopilevich, J. Appl. Mech. and Tech. Phys. **16** (6) (1975).

4. Y. I. Kopilevich, J. Appl. Mech. and Tech. Phys. **19** (1) (1978).

5. D. Z. Anderson, D.M. Lininger, and J. Feinberg, Opt. Lett. **12**, 123 (1987).

6. J. E. Ford, Y. Fainman, and S. H. Lee, Opt. Lett. **13**, 856 (1988).

7. M. Cronin-Golomb, A. M. Biernacki, C. Lin, and H. Kong, Opt. Lett. **12**, 1029 (1987).

8. M. B. Klein and R. N. Schwartz, J. Opt. Soc. Am. B **3**(2), 293 (1986).

9. S. Ducharme and J. Feinberg, J. Opt. Soc. Am. B. **3**(2), 283 (1986).

10. A. V. Nowak, T. R. Moore, and R. A. Fisher, J. Opt. Soc. Am. B **5**(9), 1864 (1988).

11. R. A. Rupp and F. W. Drees, Appl. Phys. B **39**, 223 (1986).

12. M. E. Crawford and W. M. Kays, NASA CR-2742, Nov. (1976).

13. S. B. Sutton, G. F. Albrecht, H. F. Robey, "Heat removal and optical distortions in a gas-cooled disk Amplifier," in preparation for J. ASME (1989).

14. Clifford, "The Classical Theory of Wave Propagation in a Turbulent Medium," in **Topics in Applied Physics**, Vol. 25 (1978).

15. A. M. Obukhov, Izv. Akad. Nauk. SSSR Geog. i Geofiz., **13**, 58 (1949)

16. S. Corrsin, J. Appl. Phys. **22**, 469 (1951).

17. H. F. Robey, submitted to Physical Review Letters, March (1990).

Figure Captions

1. The Schlieren Technique as a Spatial Filter

(a) Diffraction pattern of a rectangular aperture

(b) Conventional knife edge spatial filter

(c) Spatial filter tailored to the diffraction pattern

2. Optical Layout

3. The Use of $BaTiO_3$ as a Temporal Filter

4. Schematic Representation of the Flow Facility

5(a). Comparison of Measured and Computed Velocity Profiles

5(b). Comparison of Measured and Computed Wall Temperature Profiles

6. Photographs and Contours of the 2-D Spectral Density of Temperature Fluctuations at Exposure Times of a) 1/4 sec, b) 4 sec, c) 16 sec

7. Directional Spectra in the Transverse and Longitudinal Directions

A conventional Schlieren setup allows for the visualization of flow structures by spatially filtering a diagnostic beam in the Fourier transform plane

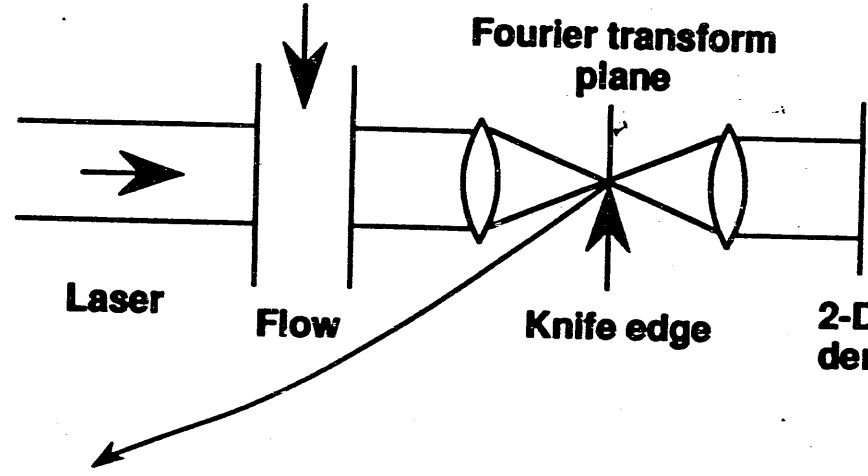

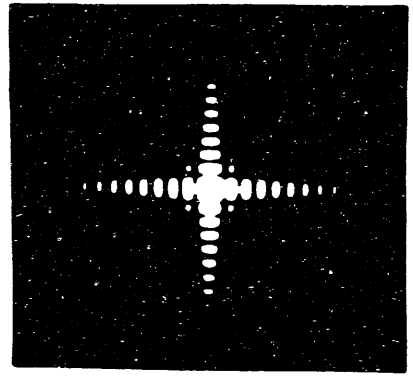

Diffraction pattern of rectangular aperture (F.T. of aperture plane)

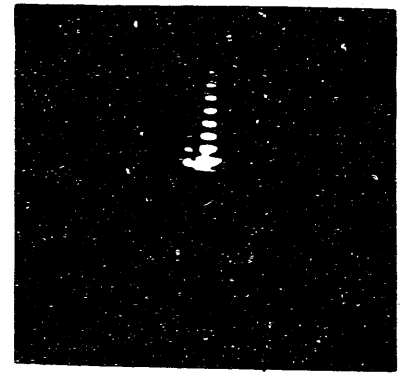

Knife edge spatial filter

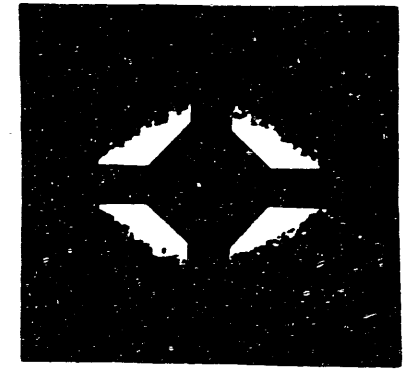

Spatial filter tailored to diffraction pattern

- The full spectrum cannot be directly obtained by this method

Optical setup for measuring turbulent spectra

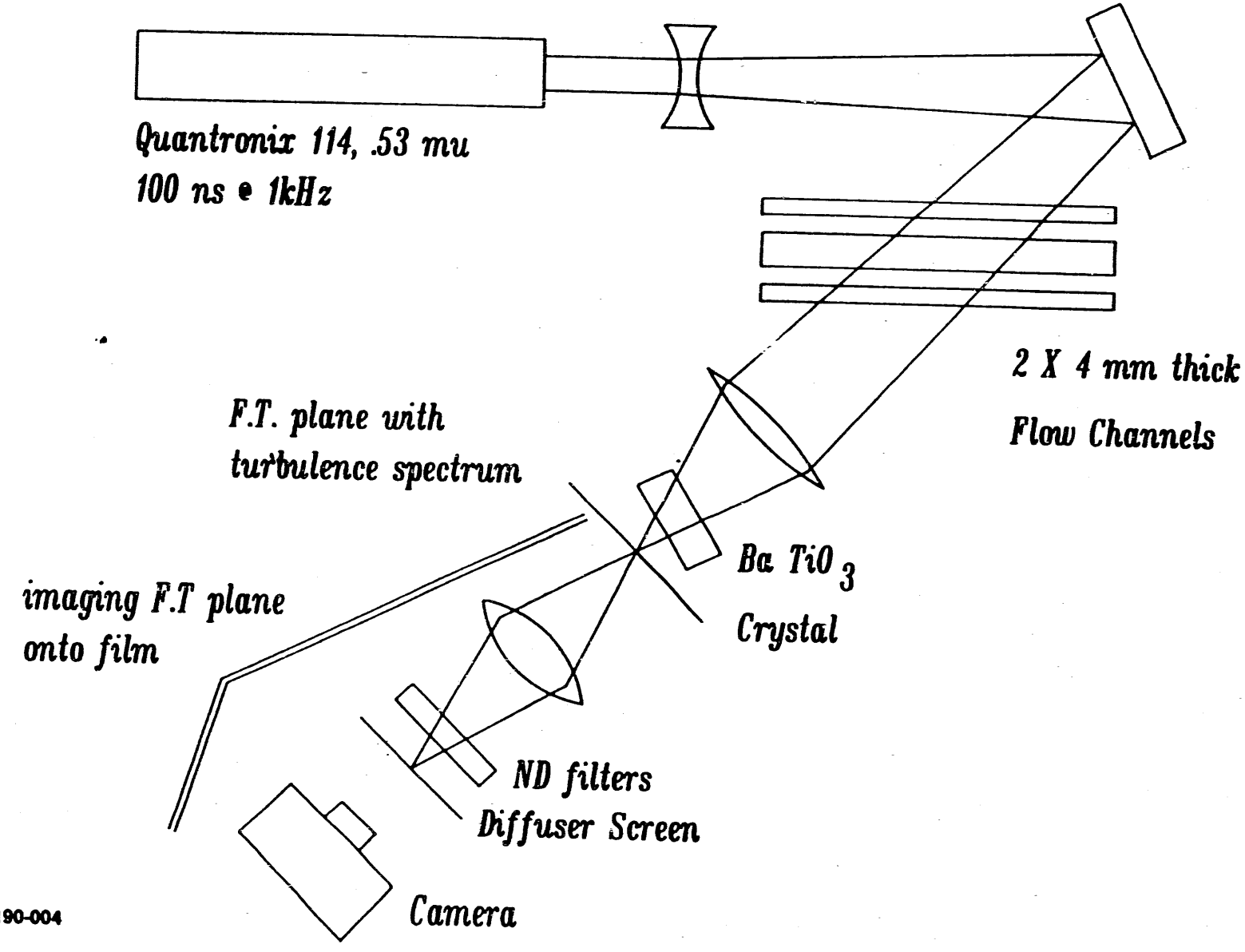

Time differentiation in $BaTiO_3$ results from the intensity-dependent growth rate of stimulated scattering from defects in the crystal

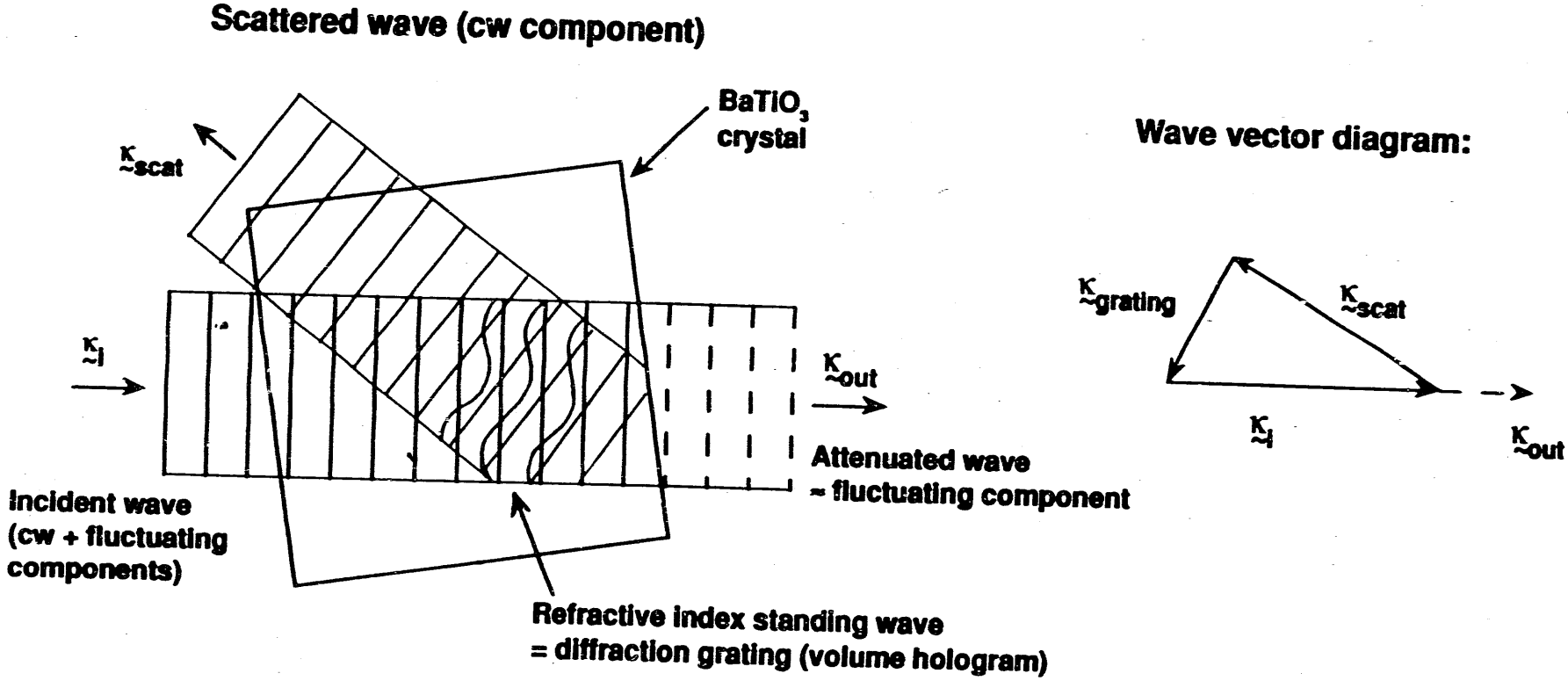

- Stimulated scattering of the cw component grows exponentially (with time constant, τ) since κ_i, κ_{scat}, and $\kappa_{grating}$ have sufficient intensity for mutual reinforcement
- Time differentiation occurs since the fluctuating component is too weak to generate much of a grating and varies too fast to allow the grating to grow

The present flow under study is a fully developed turbulent channel flow with heat addition

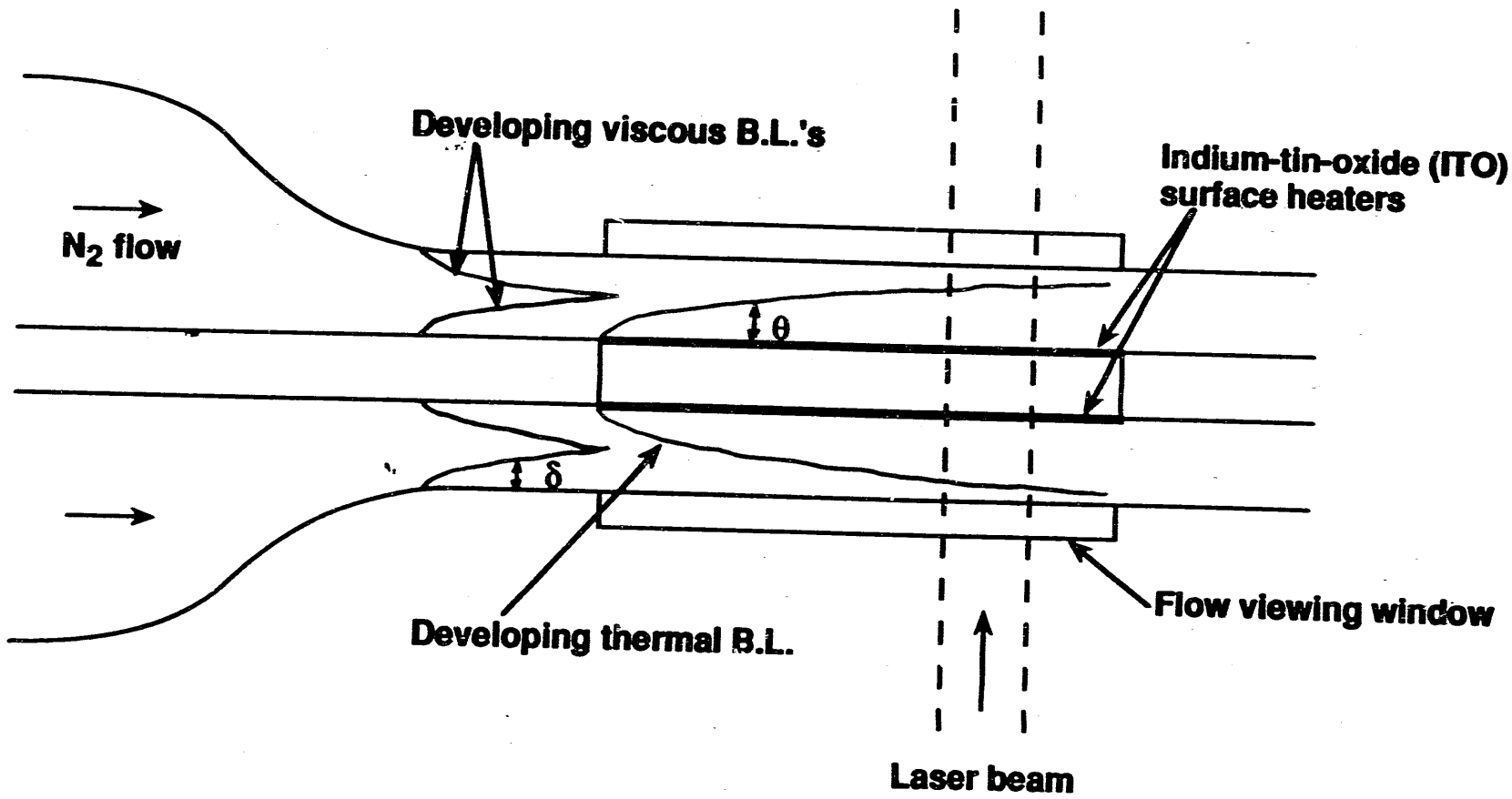

- The flow has been extensively studied by both experiment and numerical simulation

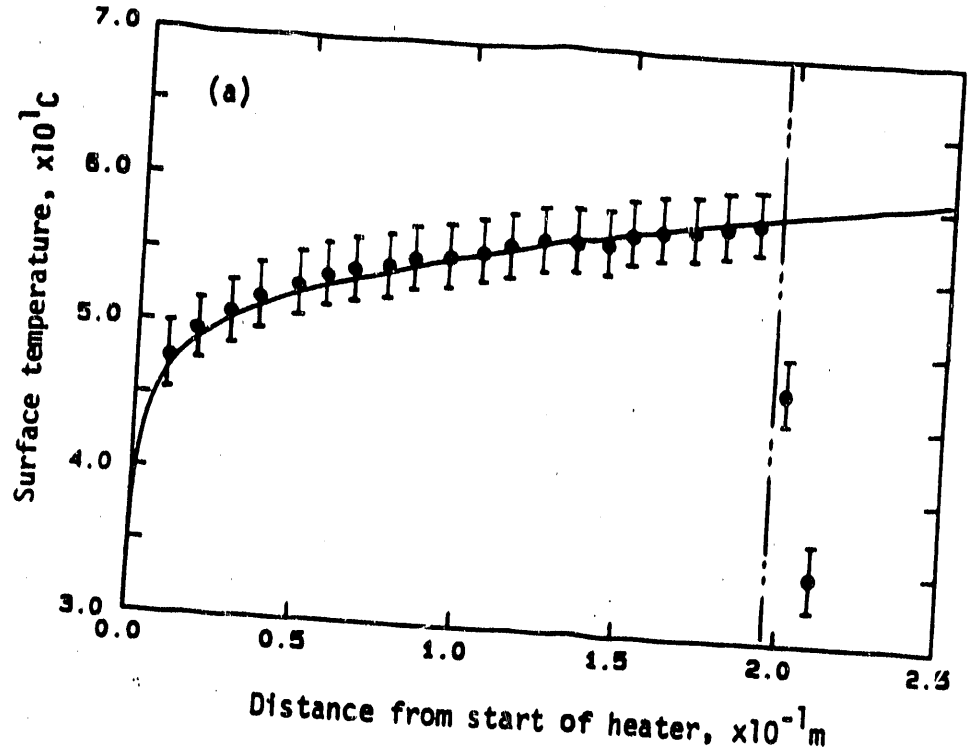

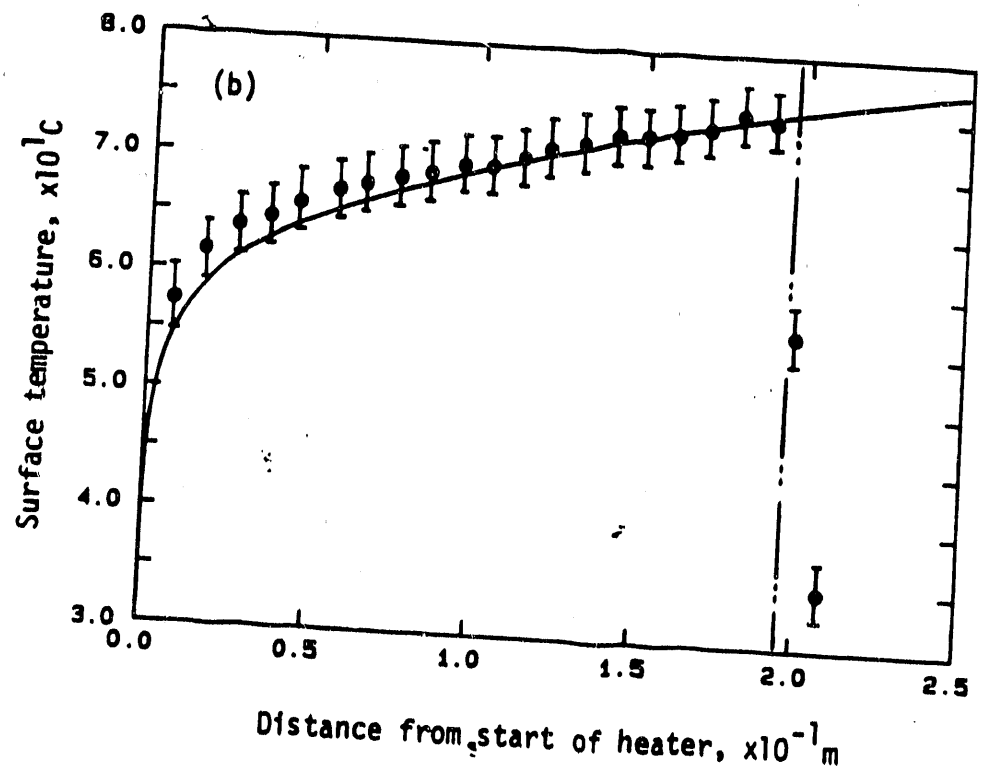

Figure 2. Surface temperatures in the LONG entry configuration. a) 1.0 W/cm^2; b) 1.5 W/cm^2

6a.

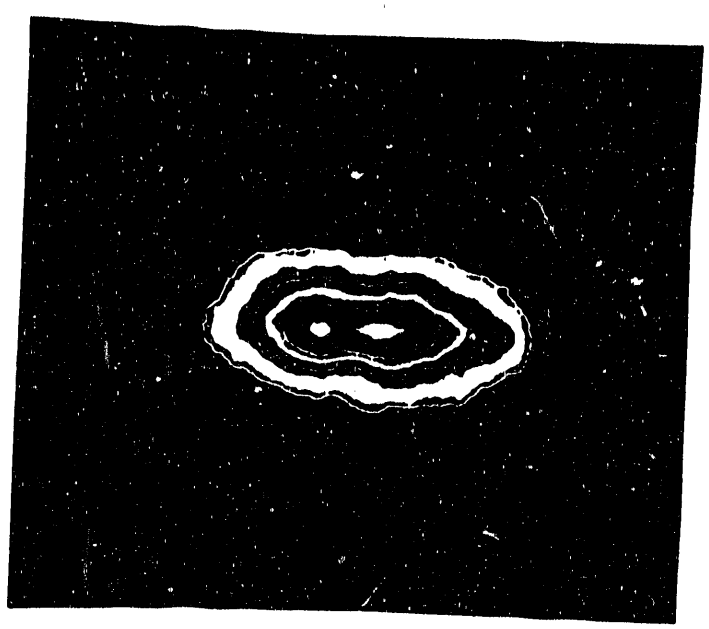

6b

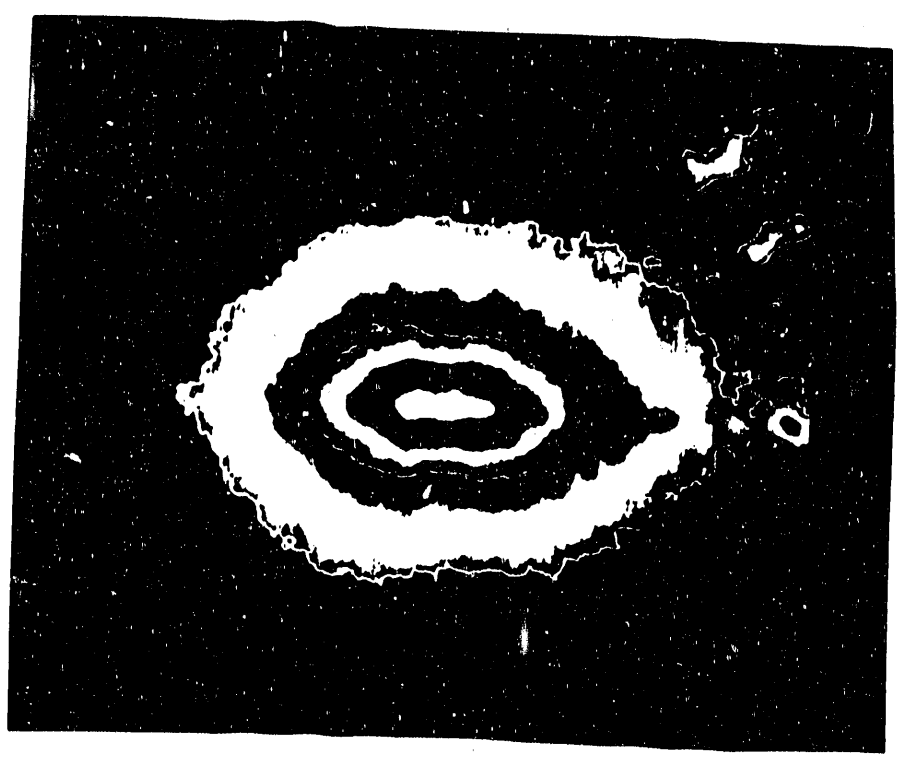

6c

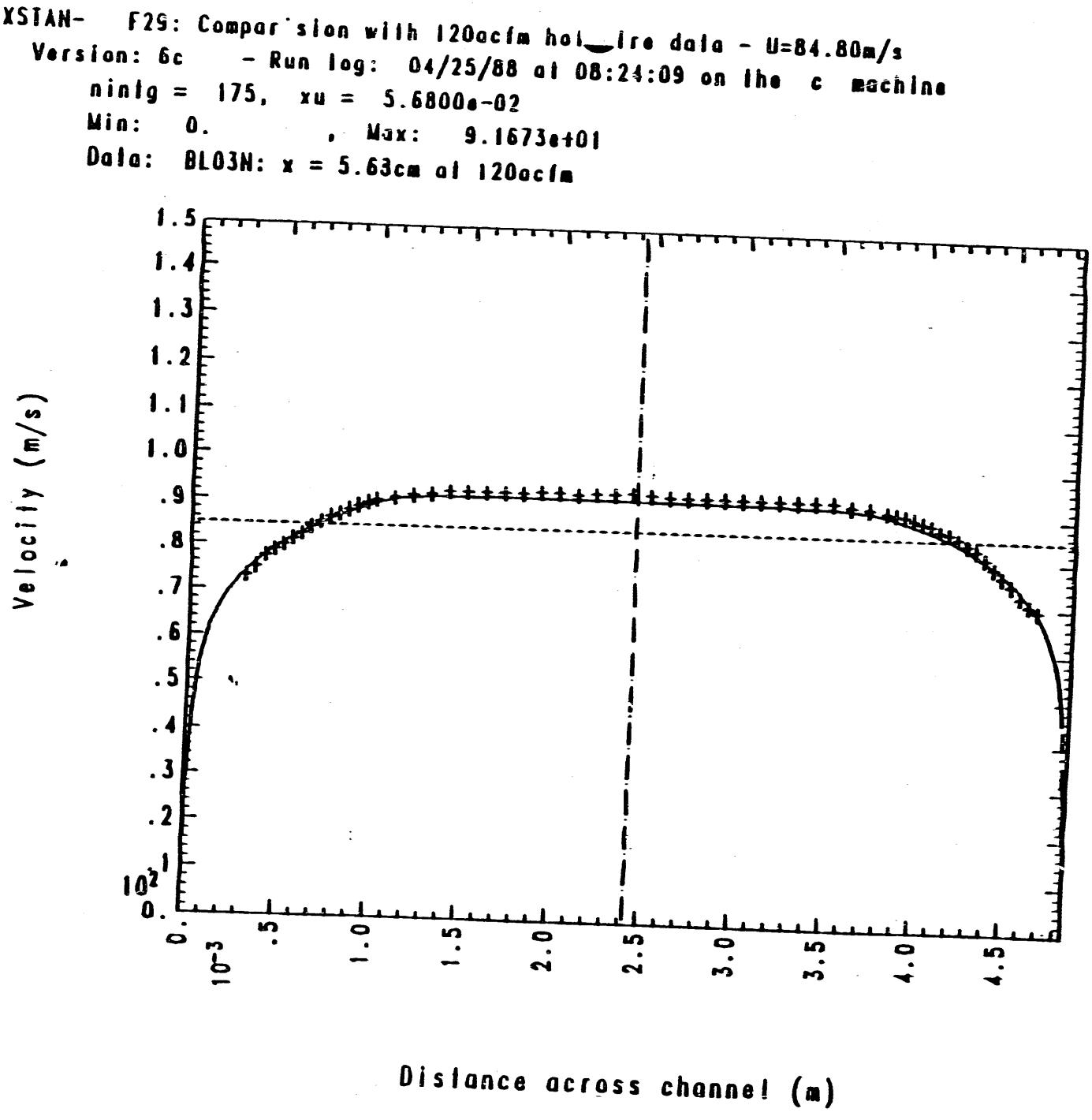

Figure 5. Comparison of Measured Velocity Profile and Profile Calculated using TEXSTAN code (= 5.69)

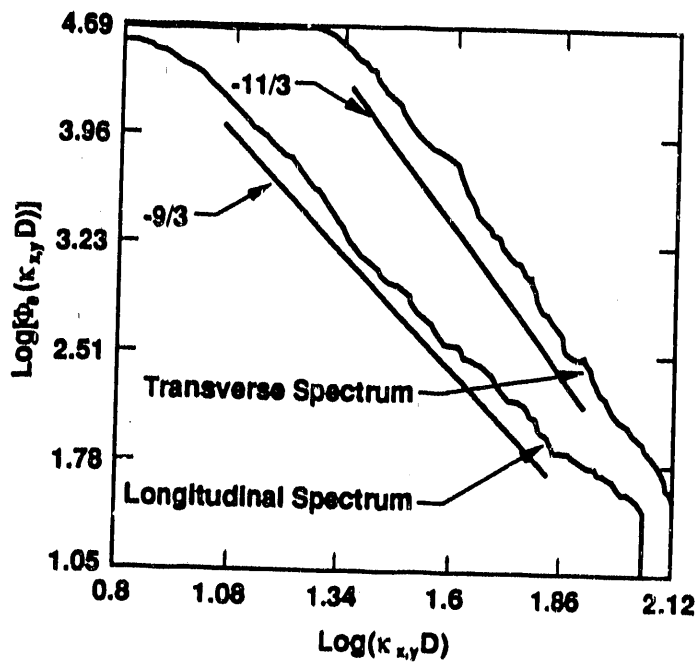
4.69
3.96
3.23
2.51
1.78
1.05
0.8
1.08
1.34
1.6
1.86
2.12
-11/3
-9/3
Transverse Spectrum
Longitudinal Spectrum
Log[Φb (κx,y D)]
Log(κx,y D)

END

DATE FILMED

01 / 22 / 91